Measurement of bistatic sea surface scattering with a parametric acoustic source

Zhiguo Yang,[1, a)] Baohua Liu,[1] Lehua Qi,[2] Paul R. White,[3] Jianghui Li,[4] Guangmin Kan,[5] and Shengqi Yu[1]

[1)] *National Deep Sea Center, Qingdao, 266237, China*[b)]

[2)] *College of Geodesy and Geomatics, Shandong University of Science and Technology, Qingdao, 266590, China*

[3)] *Institute of Sound and Vibration Research, University of Southampton, Southampton, SO17 1BJ, U.K.*

[4)] *The State Key Laboratory of Marine Environmental Science, College of Ocean and Earth Sciences, Xiamen University, Xiamen, 361102, China*

[5)] *First Institute of Oceanography, Ministry of Natural Resources, Qingdao 266061, China*

This work presents the results from a series of bistatic sea surface scattering experiments conducted in shallow water using a parametric acoustic array as a source and a receiver comprising a horizontal linear array. The experiments measured scattering at three frequencies (4, 8 and 15 kHz) and at three incident grazing angles (13°, 20° and 30°). The measurements were made over a 5 day period during which a variety of environmental conditions were encountered. This paper provides an outline of the experiments and presents some results for the forward scattering strength. The results show that the wave direction has a significant effect on the surface forward scattering. At each incident grazing angle, the fluctuations of scattering strength due to environmental conditions decreases as the frequency increases.

[a] zg.yang@163.com

[b] Also at: Pilot National Laboratory for Marine Science and Technology(Qingdao), Qingdao, 266237, China.

I. INTRODUCTION

Surface acoustic scattering is caused by the interaction of acoustic energy with the rough air-sea interface and the bubble clouds which proliferate in the region, which could have a significant impact on ocean acoustic propagation (Urick, 1983), especially in high sea states. There has been a significant amount of theoretical and experimental research which yielded empirical formulas, and theoretical expressions for modelling sea surface scattering (Thorsos and Jackson, 2012). Numerical methods, such as the integral equation method (Macaskill and Kachoyan, 1988; Thorsos and Jackson, 2012), have been developed to understand the regions of validity of scattering approximations. The Kirchhoff approximation and small height perturbation theory are two classical approaches for calculating acoustic scattering from a rough surface (Thorsos, 1988; Thorsos and Broschat, 1995). The small slope approximation (SSA), proposed by Voronovich (A.G.Voronovich, 1985), gives a systematic series expansion in terms of the generalized surface slope and has been applied to sea surfaces (Broschat and Thorsos, 1997; Thorsos and Broschat, 1995). The SSA generalizes the two classical methods in that it reduces to each in the appropriate limits of boundary roughness.

There are models of surface scattering based on a one dimensional surface model of a rough surface (A.G.Voronovich, 1985; Macaskill and Kachoyan, 1988; Thorsos, 1988; Thorsos and Jackson, 2012). Numerical methods that focus on the two-dimensional scattering problem commonly employ a isotropic rough surface (Thorsos and Jackson, 2012). However, the roughness of most natural sea surfaces is anisotropic, for instance, as a consequence of the structured nature of the gravity wave field on the sea surface. For realistic three dimensional scattering modelling, an anisotropic model of sea surface roughness is required. Three-dimensional scattering functions have been described for calculating bistatic reverberation (Ellis and Crowe, 1991). The functional form provides good quantitative agreement with measurements dominated by bottom reverberation. The initial numerical models for the study of rough surface scattering were generated in the context of electromagnetic scattering (Axline and Fung, 1978). Similarly, methods for predicting bistatic scattering from two-dimensional conducting random rough surfaces at millimeter-wave frequencies have been developed (Chan *et al.*, 1996) and are applicable to scattering problems in underwater acoustics. Gauss (Gauss *et al.*, 2005, 2002) presented a semi-empirical broadband surface scattering strength formula parameterized environmentally by the scattering angles, wind speed and two surface-wave spectral parameters. By applying physical principles, a new bistatic scattering strength model was developed that allows extrapolation in frequency and extends to most three-dimensional geometries.

Dahl (Dahl, 1996, 2001, 2004) conducted experiments to measure the spatial coherence of sound forward scattered signal from a two-dimensional rough sea surface. The coherence was measured at high frequency with a linear array oriented transverse to the direction of propagation, giving estimates of the horizontal coherence at near specular angles from in-plane angles. At the same time, surface scattering strength out-of-plane was explored (Dahl, 1999). The results show both the coherence of forward acoustic scattering and its strength, decreased with increasing distance out-of-plane from the specular point. Different model calculations of the bistatic cross section of the sea surface agreed well with the data. These experiments used omnidirectional acoustic sources. The use of a directional acoustic source allows more accurate study of the scattering strength as a function of grazing angle, and the azimuthal dependence of the forward scattering strength in a bistatic configuration can be explored. Zornig (Zornig, 1978) conducted a series of high frequency experiments in a water tank at a variety of grazing angles, azimuth angles and wind speeds, with a directional projector at frequencies of 1.1 MHz and 1.3 MHz. The results suggest that the bistatic scattering strength at high frequencies is not strongly dependent on root-mean-square (RMS) wave height, but did depend on other factors including the RMS slope, probability density function (PDF) of slopes, or correlation distance caused by both wind speed and its direction. Some of the surface acoustic scattering data were compared with a time-domain version of the facet-ensemble method and showed good agreement (Kinney and Zornig, 1985). Similar results were obtained for bistatic radar scattering from a rough sea surface, and it was demonstrated that the bistatic scattering exhibits a sensitivity to wind direction (Voronovich and Zavorotny, 2013). For low and mid-frequency (< 20 kHz) acoustic signals, it is hard to conduct such experiments in a laboratory. In this paper, we use a parametric array with a very narrow beam pattern as an acoustic source to conduct a series of measurements in the ocean to measure the three-dimensional forward scattering and the dependence of the scattering on the wave direction of the sea surface.

This paper is organized as follows. The experiments are described in Sec.II, and the calibrations of the transmitting system and receiving system are presented in Sec.III. SectionIV describes the methodology for the forward scattering calculation. The results are discussed in Sec.V and conclusions are drawn in Sec.VI.

II. EXPERIMENTAL SETTING

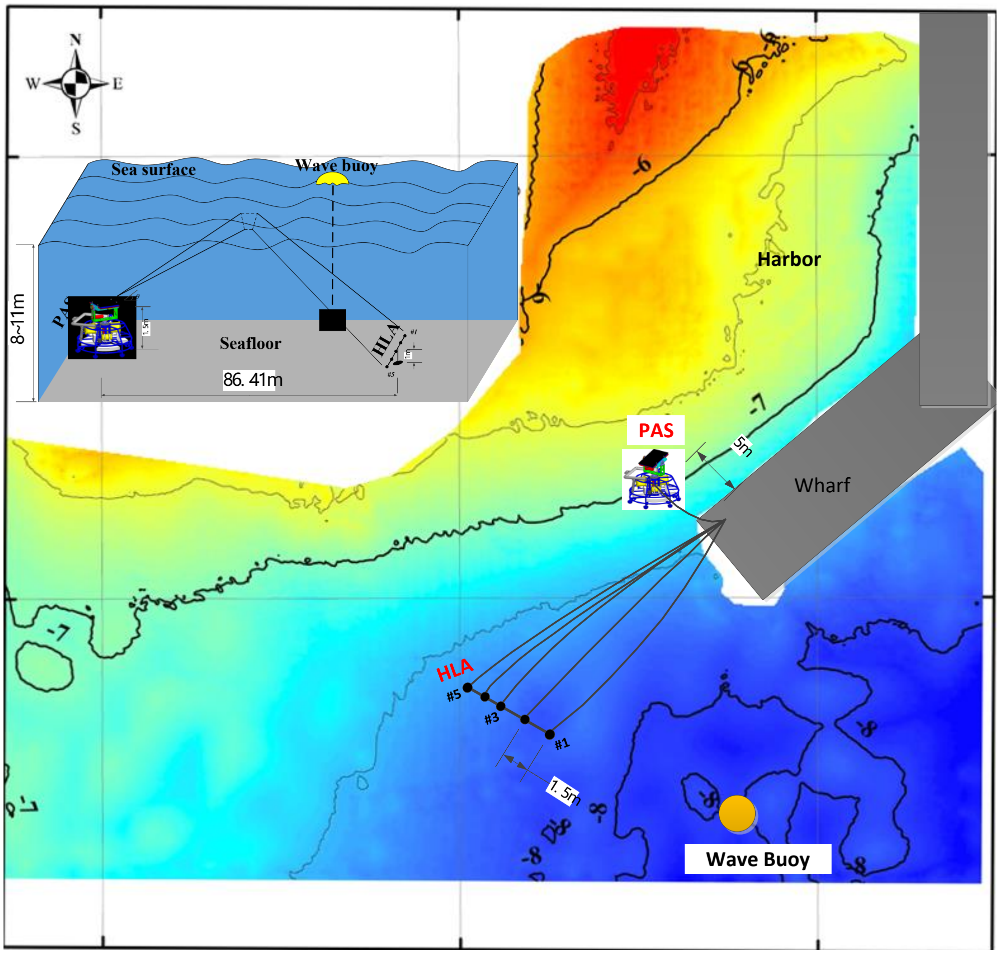

FIG. 1. Experimental layout of the bistatic three-dimensional forward-scattering measurement. The parametric array source (PAS) is deployed beside the wharf. The HLA consisting of five hydrophones is shown as black dots. A wave buoy, indicated by a yellow circle, is deployed at a range of 100 m from the HLA. The insert figure illustrates the three-dimensional geometry of the experiments.

The experiment was conducted between 25th and 30th October 2019, offshore Qingdao, China. The water depth varied between 8 m and 11 m under the influence of tidal variations.

Figure 1 shows an overview of the experimental configuration. An acoustic parametric array source (PAS) was used to generate acoustic signals from 4 to 15 kHz. The forward-scattering signals were received by a horizontal linear array (HLA), which was nearly perpendicular to the direction of the incident wave. The experimental site was located in front of a wharf facing the ocean. The PAS was operated via a cable linked to a control system. In the upper left of the Fig. 1, the experimental geometry for measuring forward-scattering by the sea surface is sketched. The PAS was deployed on the sea floor with its center 1.5 m above the seabed and installed on a rigid frame to adjust the azimuth via an electronic motor. A depth sensor and a compass were used to monitor source depth and array azimuth and pitch attitude. The incident grazing angle (θ_i, see Fig. 7) of the forward scattering measurement was adjusted by electronic steering of the vertical beam of the PAS. The vertical beam of the PAS could be steered $\pm 20°$, which corresponds to incident grazing angles of forward-scattering from 5° to 45° when deployed on the sea floor. During the experiment, signal frequencies of 4, 8 and 15 kHz were transmitted at incident grazing angles of 13°, 20° and 30°, respectively. The HLA was deployed 1 m above the sea floor. The range between the HLA and the PAS was 86.41 m. A wave buoy was deployed at a range of approximately 100 m from the experimental site. The outputs of the wave buoy include major wave direction, distribution of the wave direction, significant wave height and maximum wave height, with an output period of 20 minutes. Wind speed was recorded every 2 minutes at a meteorological station within 300 m of the experimental site at an altitude of 10 m. Conductivity, temperature, and pressure (CTD) profiles were collected within one hour after each measurement. These data showed that the water column was well mixed down to the bottom, with an average sound speed of 1517 m/s. The physical properties of surficial sediment including mean grain size and density were analyzed. The sediment has mean grain size 2.5 μm, density 1.414 g/cm^3, attenuation 0.057 dB/m/kHz, and sound-speed ratio 0.973. Based on these results, the sediment could be described as silty clay.

The PAS used in the experiment comprises 896 directional transmit elements, organized as 32 uniform linear arrays each of 28 elements. The primary frequency of the PAS is 40 kHz. The secondary signals from 1 to 20 kHz are modulated onto the primary frequency. The beamwidth of the PAS is extremely narrow relative to the transmitter aperture and is about 3° in both the horizontal and vertical directions (see Sec. III).

III. SYSTEM CALIBRATION

A. Parametric array source calibration

The calibration of the parametric array was performed in a 50 × 15 × 10 m ($L \times W \times D$) anechoic tank. Two mobile trolleys equipped with mounting stations were used to install the parametric array and the receiver. Figure 2 shows a photograph of the parametric array installed on the trolley in the anechoic tank and on a rigid frame in the sea experiments. After installation on the first mounting station in the anechoic tank, the parametric array was lowered to a depth of 5 m, in the middle of the tank. A hydrophone (TC4033: sensitivity -203 dB re 1 V/μPa) was also lowered to the same depth after being fixed on the second mounting station. The second station moved during calibration that allowing maximum separated ranges between parametric source and receiving hydrophone up to 40 m.

FIG. 2. Photographs of the parametric array after installation on the mounting station. The left sub-figure shows that the PAS was installed on the mounting station then rotated horizontally to measure the vertical beam pattern. The PAS was installed on a rigid frame in the sea experiments, which is shown in the right sub-figure.

The source level and beamwidth of a parametric array are range dependent. The calibration was performed at different ranges to obtain the source level and beamwidth at ranges corresponding to the near field and far field. The parametric array, which was initially mounted on its side, can be rotated 180° horizontally to measure the vertical beamwidth after mounting on the station. Then the horizontal beamwidth of the parametric array was measured after re-mounting the parametric source on the station vertically. After fixing the PAS, a hydrophone was mounted to the second station and lowered to the same depth as the PAS. The source level at primary frequency of 40 kHz was about 240 dB re 1 μ Pa @ 1 m, which is 40 dB greater than that of the difference frequency signal. An analogue notch filter is used to attenuate the primary signal to mitigate issues associate with the signal's dynamic range. The central frequency of the notch filter is 40 kHz, and the amplitude attenuation is 40 dB. Then a digital band-pass filter with a bandwidth of 1 kHz, centred on the difference frequency, was used to obtain the desired signal at that frequency. The on-axis sound pressure level (SPL) and the beam pattern at difference frequencies of 4, 8 and 15 kHz at ranges from 5 to 40 m were measured. Signals were transmitted at a period of 2 s with a pulse duration of 2 ms for each difference frequency. To measure the beam pattern, the mounting station, where the PAS was installed, was rotated about its vertical axis. Source levels computed at difference frequencies of 4, 8 and 15 kHz are shown in FIG. 3. This shows that the source level at the difference frequency is not constant at ranges less than 20 m. This is because the source level for a parametric array is range dependent if measured within the interaction zone (Moffett and Mellen, 1977).

The beam patterns for several frequencies at a range of 35 m are shown in FIG. 4. Both the horizontal and vertical beam patterns of the array become narrower as the frequency increases. The beam patterns for a difference frequency of 8 kHz at ranges of 10 to 40 m are shown in FIG. 5. This demonstrates that both horizontal and vertical beam patterns become narrower as the range increases, with the effect diminishing with range, so that above 20 m the beamwidth can be regarded as constant with range. In the experiments, the slant ranges from the PAS to the ensonified region were approximately 20, 30 and 38 m for incident grazing angles of 30°,20° and 13° respectively.

The azimuth of the PAS was controlled using mechanical steering, whilst electronic steering was used to change incident grazing angles. When the PAS is steered electronically, the SL (measured in the direction of the beam) changes as a consequence of the directivity of the transmit elements. The SL, at 8 kHz, was measured as the beam steered vertically and

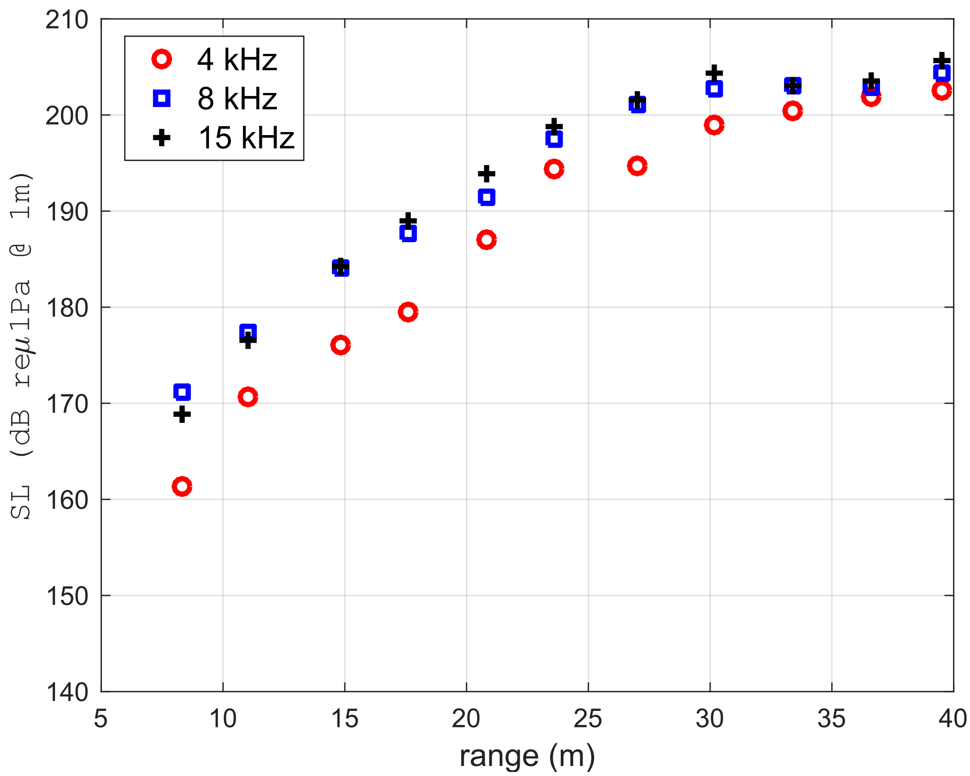

FIG. 3. Source level calibration results as a function of range for 4 (circles), 8 (squares) and 15 kHz (crosses).

the results are shown in FIG. 6. The SL changes by less than 2 dB when the beam is steered within ±15°, whereas outside that region more significant changes were observed. In these experiments, the electronic beam was steered to 11°, 4° and −6° for the incident grazing angles of 13°, 20° and 30° respectively.

B. Calibration of the receiving array

The HLA was constructed using five hydrophones (sensitivity -196 dB re 1 V/μPa.) mounted on a 6 m frame, the spacings between the elements were 1.5 m, 1.5 m, 0.92 m and 0.58 m. As in the tank measurements both a notch filter and a low-pass filter were applied

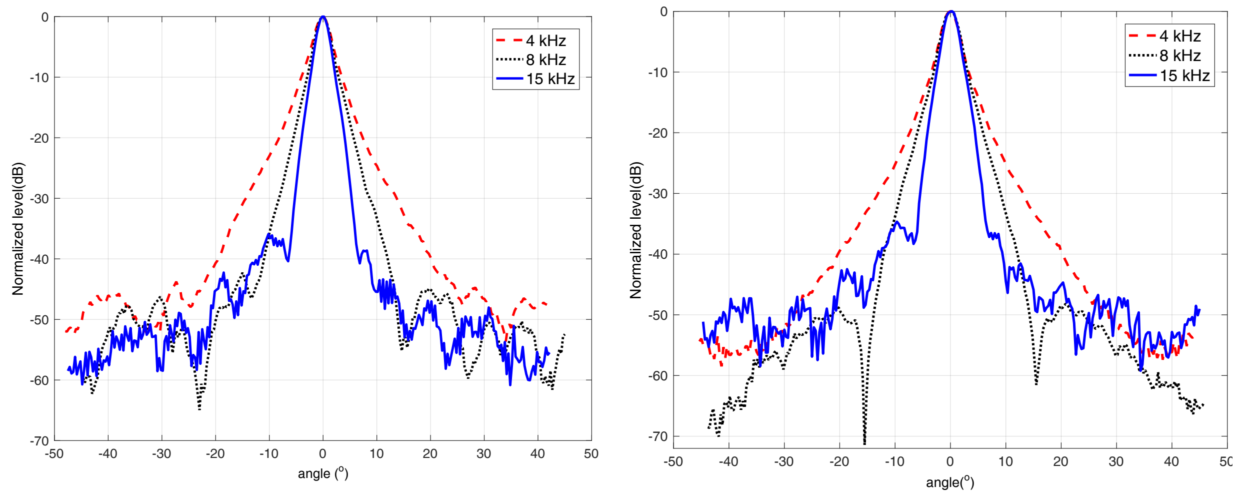

(a)vertical beam pattern (b)horizontal beam pattern

FIG. 4. Beam patterns of different frequencies at a range of 35 m. Both the vertical and horizontal beamwidth tend to become narrower as the frequency increases.

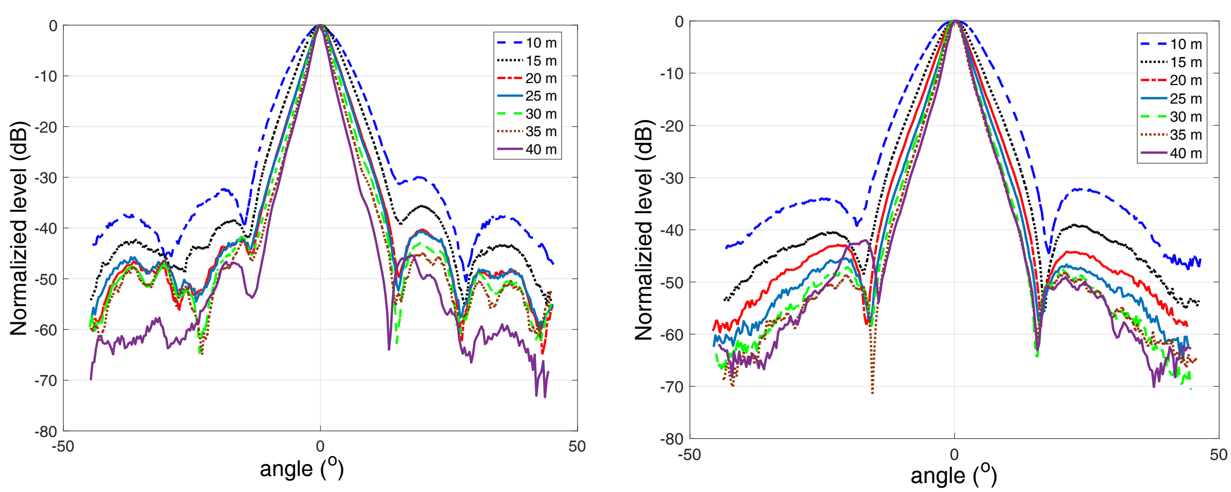

(a) vertical beam pattern (b) horizontal beam pattern

FIG. 5. Beam patterns at 8 kHz at ranges from 10 m to 40 m. The beam pattern depends on range at distances less than 20 m.

to hydrophone signals to attenuate the primary signal prior to the application of 20 dB gain via a pre-amplifier.

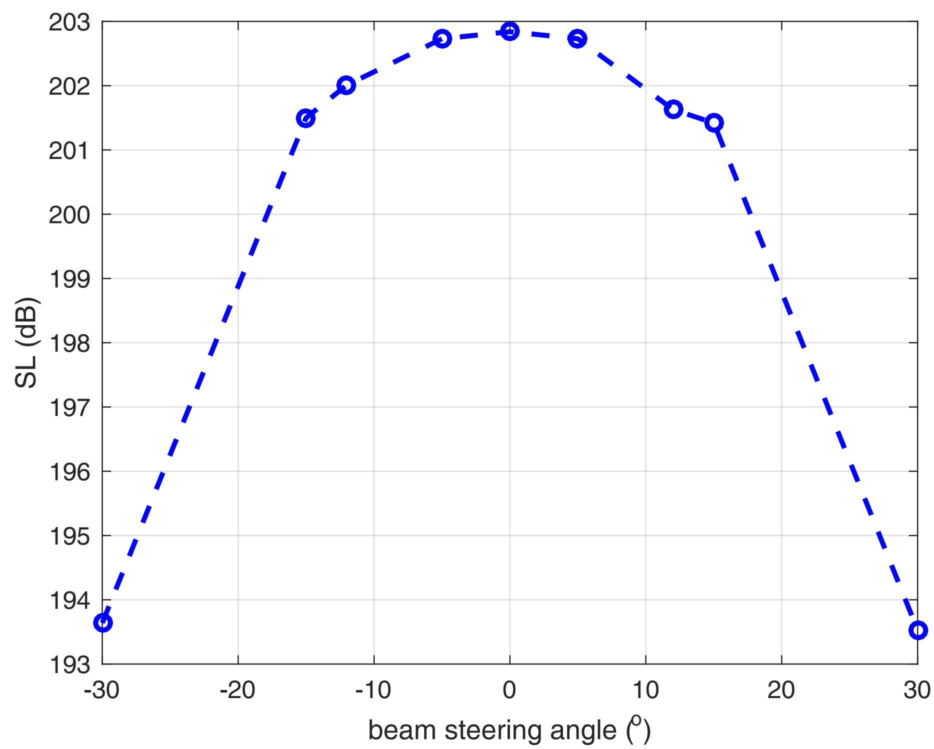

FIG. 6. Source level with electronic beam steering at 8 kHz. The source level is 202.8 dB without beam steering, and it drops to 201.5 dB and 193.5 dB when the beams are steered to ±15° and ±30° respectively.

The HLA was connected, via a cable, to the same shore based controller as the PAS allowing synchronous data transmission and collection. This allowed the positions of the hydrophone elements to be determined relative to the source. This was achieved by firstly, steering the beam of the PAS so that it was horizontal. Then, the PAS was rotated horizontally so that it pointed at hydrophone No. 2 of the HLA. The PAS was then rotated so that the amplitude of the signal from hydrophone No. 2 was maximised and then steered vertically to confirm that the beam axis was directed at the chosen hydrophone. Then the travel times between the PAS and the HLA could be used to compute the relevant distances.

IV. 3-D FORWARD SCATTERING MEASUREMENTS

A. Calculation method of forward scattering strength

The geometry of the experiments is shown in FIG. 7. θ_i and θ_s are incident grazing and scattered grazing angles measured from the horizontal, ϕ_i and ϕ_s are incident and scattered azimuth measured relative to the wave direction, r_i and r_s are the slant ranges from the source to the ensonified region and the ensonified region to the receiver.

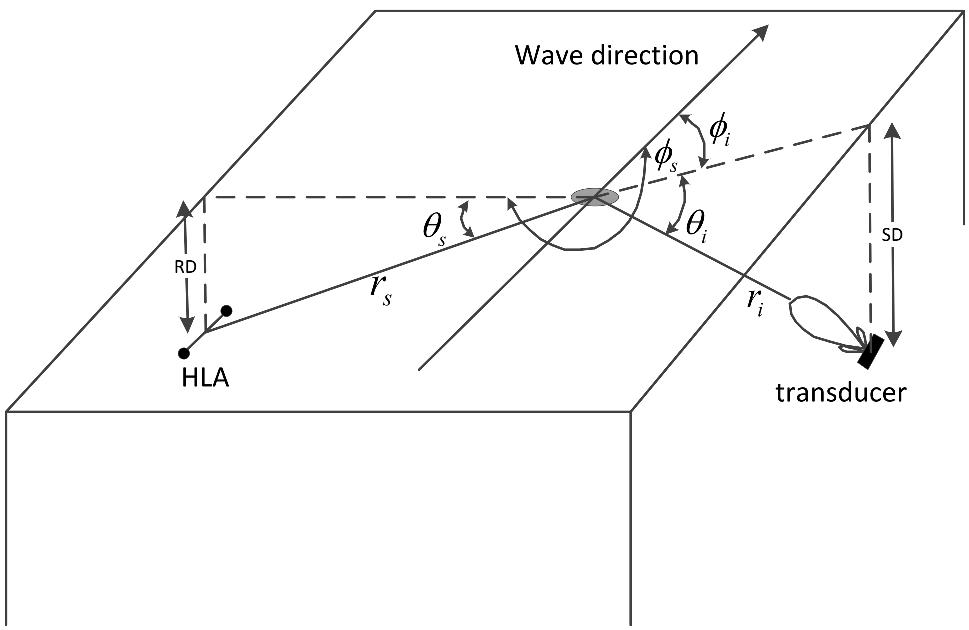

FIG. 7. Geometry of the forward scattering measurement. Incident azimuth ϕ_i and scattered azimuth ϕ_s are defined relative to the surface wave direction. Incident grazing angle θ_i and scattered grazing angle θ_s are defined relative to the sea surface.

For signals at frequencies between 1 kHz and 20 kHz, the acoustic absorption coefficient in the seawater is less than 2 dB/km (Urick, 1983). The largest slant range in the series of measurements is about 40 m, so the effects of absorption were not considered. Therefore, transmission loss calculations only accounted for spreading losses based on a spherical spreading model. We consider the scattering from a small area A, such that the changes of r_i and r_s over the area A is small. Therefore, the average squared pressure output of the receiver before being amplified over the pulse duration for the nth pulse as $\bar{p}_n(\tau)^2$ can be expressed as (Yu *et al.*, 2017)

$$\left\langle \bar{p}_n(\tau)^2 \right\rangle = \frac{I_0 {r_0}^2}{{r_i}^2 {r^2}_s} \int \sigma\left(\theta_i, \phi_i, \theta_s, \phi_s\right) b_t\left(\theta_i, \phi_i\right) b_r\left(\theta_s, \phi_s\right) dA, \tag{1}$$

where the symbol $\langle \bullet \rangle$ denotes the averaging over all independent transmitted pulses, $\bar{p}(\tau)$ means take an average over a time interval equal to the pulse length τ, I_0 is the incident intensity of the source at a range of r_0, $\sigma\left(\theta_i, \theta_s, \phi_i, \phi_s\right)$ is the forward scattering cross section at incident grazing angle θ_i, incident azimuth ϕ_i, scattered grazing angle θ_s and scattered azimuth ϕ_s, $b_t\left(\theta_i, \phi_i\right)$ and $b_r\left(\theta_s, \phi_s\right)$ are three-dimensional beam pattern functions of the source and receiver respectively, and dA is the differential element of the ensonified area determined by the beam patterns of source and receiver.

The SL is the source level in dB re 1μPa m and defined as $SL = 10\log_{10}\left(I_0 {r_0}^2\right)$. Considering the change in both incident and scattered grazing angles and azimuths are small enough that $\sigma\left(\theta_i, \phi_i, \theta_s, \phi_s\right)$ is approximately constant over the ensonified region. Taking $10\log_{10}$ of both sides of the equation, we obtain the sonar equation used to calculate the three dimensional surface scattering as a function of incident angle, incident azimuth, scattering angle and azimuth

$$S(\theta_i, \phi_i, \theta_s, \phi) = 10\log_{10}\left\langle \bar{p}_n(\tau)^2 \right\rangle - SL + TL_{in} + TL_{out} - 10\log_{10} A, \tag{2}$$

where $S(\theta_i, \phi_i, \theta_s, \phi)$= $10\log_{10}\sigma\left(\theta_i, \phi_i, \theta_s, \phi_s\right)$ is the surface forward scattering strength in dB. $TL_{in} = 20\log_{10} r_i$ is the transmission loss from the source to the ensonified region and $TL_{out} = 20\log_{10} r_s$ is the transmission loss from ensonified region to receiver. Here the beam pattern $b_t\left(\theta_i, \phi_i\right)$ is approximated using an idealised beam pattern which is unity within the main beam (ensonified area) and zero outside, $b_r\left(\theta_s, \phi_s\right)$ is unity for the omnidirectional receiver used in the experiments. The boundary between these two ensonified areas is selected to correspond to the -3 dB points on the beam patterns measured in Sec. III A. This would introduce an approximation error less than 3 dB. The ensonified area A is calculated based on geometric projection of an idealised beam pattern in Sec. IV B.

B. Ensonified area calculation

The radiation pattern for the rectangular planar parametric array is considered as a cone. When it intersects with the sea surface, the corresponding projective figure is an ellipse. The center of ensonified region is defined as the origin of a geodetic coordinate system with the mean sea surface defining the xoy plane (FIG. 8). In this system θ_i represents the incident grazing angle.

Rotating the geodetic coordinate system $o-xyz$ by θ_0, we obtain the source and receiver coordinate system $o-x'y'z'$. Both coordinate systems share the same y axis, thus we only show the xoz planes here.

The cone is determined by the beam pattern of the array according to

$$(z' - r_i)^2 = k_V^2 x'^2 + k_H^2 y'^2 \tag{3}$$

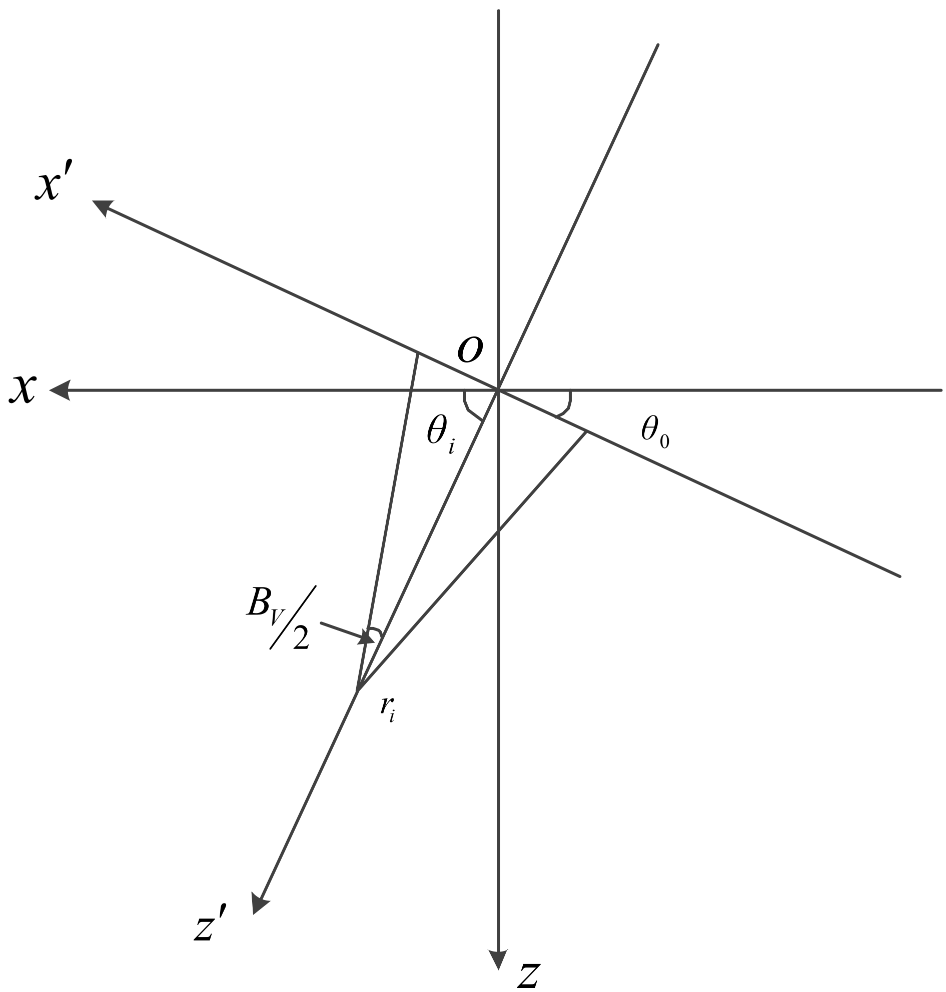

FIG. 8. Coordinate transformation used to calculate the ensonified area. The xoy plane represents the sea surface. Both coordinate systems have the same y axis, and only the xoz plane is shown here.

where $k_V = \cot(B_V/2)$ and $k_H = \cot(B_H/2)$ in which B_H and B_V are the -3 dB beamwidths of the PAS in the horizontal and vertical directions respectively.

The mapping relationship between the two coordinate systems is

$$\begin{cases} x' = x\cos\theta_0 + z\sin\theta_0, \\ y' = y, \\ z' = z\cos\theta_0 - x\sin\theta_0, \end{cases} \tag{4}$$

where $\theta_0 = \pi/2 - \theta_i$. In $o-xyz$, the cone is described by

$$(z\cos\theta_0 - x\sin\theta_0 - r_i)^2 = k_V^2(x\cos\theta_0 + z\sin\theta_0)^2 + k_H^2 y^2. \tag{5}$$

To calculate the ensonified area, let $z = 0$, then the projective figure corresponding to conics on plane xoy is

$$\left(-x\sin\theta_0 - r_i\right)^2 = k_V^2\left(x\cos\theta_0\right)^2 + k_H^2 y^2. \tag{6}$$

The equation is then transformed to

$$\frac{x^2\left(k_V^2\cos^2\theta_0 - \sin^2\theta_0\right)}{{r_i}^2} - 2x\frac{\sin\theta_0}{r_i} + \frac{k_H^2}{{r_i}^2} = 1. \tag{7}$$

Given $D = \frac{k_V^2\cos^2\theta_0 - \sin^2\theta_0}{{r_i}^2}$, substituting it to the Eq.(7) and dividing both sides of the equation by D, we obtain

$$x^2 - 2x\frac{\sin\theta_0}{r_iD} + \left(\frac{\sin\theta_0}{r_iD}\right)^2 + \frac{k_H^2}{{r_i}^2D}y^2 = \frac{1}{D} + \left(\frac{\sin\theta_0}{r_iD}\right)^2, \tag{8}$$

which can be written in the form of the equation for an ellipse

$$\frac{\left(x - \frac{\sin\theta_0}{r_iD}\right)^2}{a^2} + \frac{y^2}{b^2} = 1, \tag{9}$$

where $a = \sqrt{\frac{1}{D} + \left(\frac{\sin\theta_0}{r_iD}\right)^2}$, and $b = \frac{\sqrt{{r_i}^2 + \frac{\sin^2\theta_0}{D}}}{k_H}$. The area of the ellipse being

$$A = \pi ab. \tag{10}$$

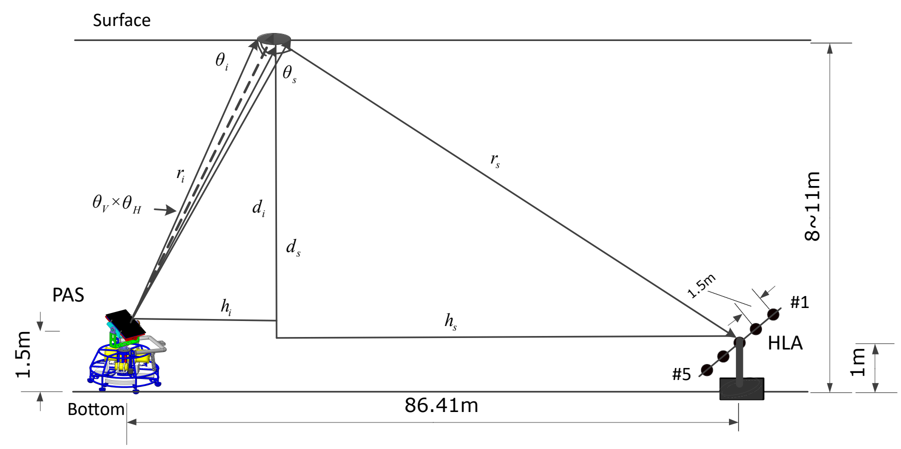

(a) Bistatic forward surface scattering measurement geometry

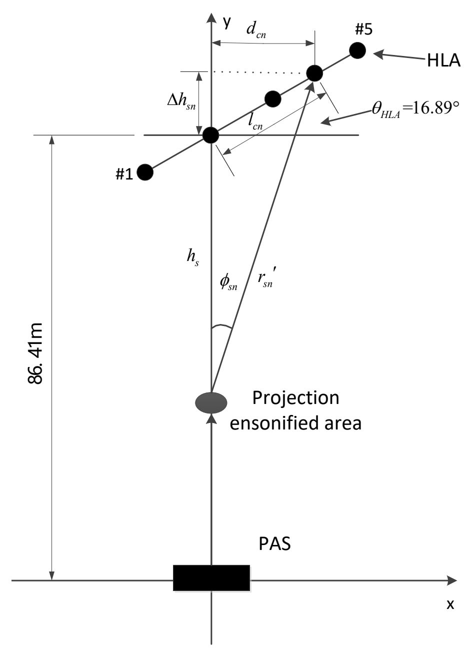

(b) Geometry projected on the sea floor

FIG. 9. Scattering geometry and key variables. The variables are labelled on the figure. The range between the PAS and the reference element in the HLA is 86.41 m, and θ_{HLA} is 16.89°.

C. Calculation of scattering grazing angle and azimuth

The bistatic forward surface scattering measurement geometry is shown in FIG. 9. As discussed in Sec. IV A, the beam pattern $b_t(\theta_i, \phi_i)$ approximated using an idealised ellipsoidal beam pattern which is unity within the B_H and B_V and zero outside. When the beam is pointed to a desired direction via electronic steering, the beam width and side-lobe structure of the beam pattern change (Elliott, 1963). Various values of B_H and B_V are used according to the calibration results in Sec. III A at different frequencies, incident grazing angles and ranges. Note that the value of B_V changes with vertical steering angle, and the value of B_H does not change with horizontal angle, but only changes with transmitting frequency, since horizontal steering is achieved mechanically, not electronically. θ_i and θ_s are incident grazing angle and forward scattering grazing angle. θ_i is given by a compass installed on the PAS. The scattering grazing angle θ_s is given by

$$\theta_s = 180 - \tan^{-1}\left(\frac{d_i + 0.5}{86.41 - h_i}\right) \tag{11}$$

where d_i and $d_i + 0.5$ are the depth of the PAS and the HLA respectively, and h_i is the horizontal range from PAS to the ensonified area $h_i = d_i/\tan\theta_i$.

In order to calculate the scattering azimuth of each hydrophone, the experimental geometry shown in FIG. 1 is projected on the sea floor. Geometry and variables are shown in FIG. 9(b). Here the l_{cn} is the distance from hydrophone No. 2 of the HLA to the nth hydrophone. Then the azimuth of the nth hydrophone is given by

$$\phi_{sn} = \tan^{-1}\left(\frac{l_{cn}\cos\theta_{HLA}}{h_s + l_{cn}\sin\theta_{HLA}}\right) \tag{12}$$

where h_s is the horizontal range from the ensonified region to hydrophone No. 2 of the HLA, and here $h_s = 86.41 - h_i$, θ_{HLA} is the angle between the HLA and the direction perpendicular to the incident wave.

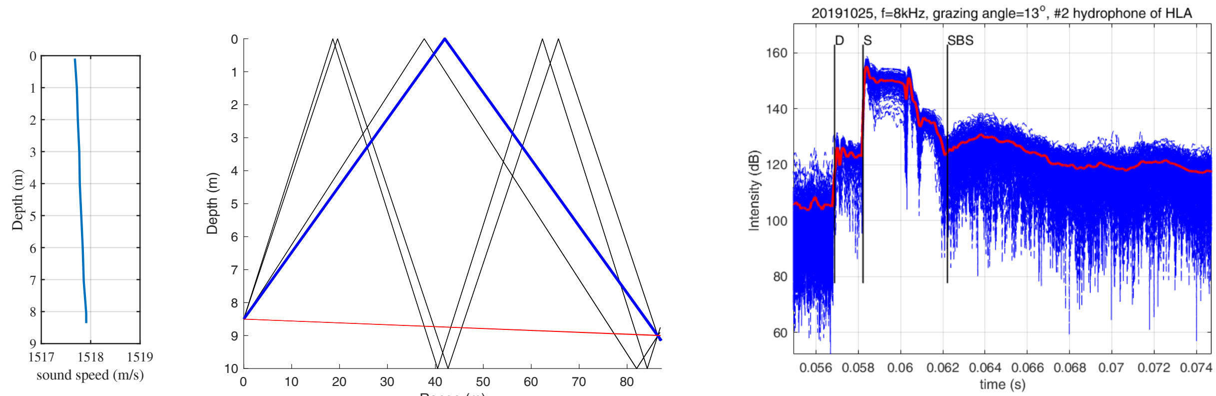

(a) SSP

(b) Dominant ray paths

(c) Intensity average of the envelope of the received signals

FIG. 10. Bellhop ray trace model results and scattering signals from experiment on October 25 at incident grazing angle of 13°. The blue curves in (c) are all the independent samples corresponding to each ping and the red curve is the mean value.

The time arrivals of scattering signal for the HLA are estimated based on the geometry shown in FIG. 9 and compared with the results of the Bellhop ray tracing model. A typical result of the Bellhop model is based on the sound speed profile (SSP) collected in the same area on 25th October, 2019 (FIG. 10(a)). FIG. 10(b) shows dominant ray paths for an incident grazing angle of 13°. In FIG. 10(c) direct arrival (D), surface (S) bounce and surface-bottom-surface (SBS) bounce calculated based on the geometry shown in FIG. 9 are labelled on an intensity average of signals of hydrophone No. 2 of the HLA at a frequency of 8 kHz corresponding to an incident grazing angle of 13°. The surface interaction signals are readily identified. Simulations were run with the bottom acoustic properties given in Sec. II for a flat interface. Only S and SB path are considered. Different receiving signals of different receiver heights were compared with the real receiving signal of the hydrophone No. 2 at 8 kHz at same incident grazing angle in FIG. 11. The results show that the change

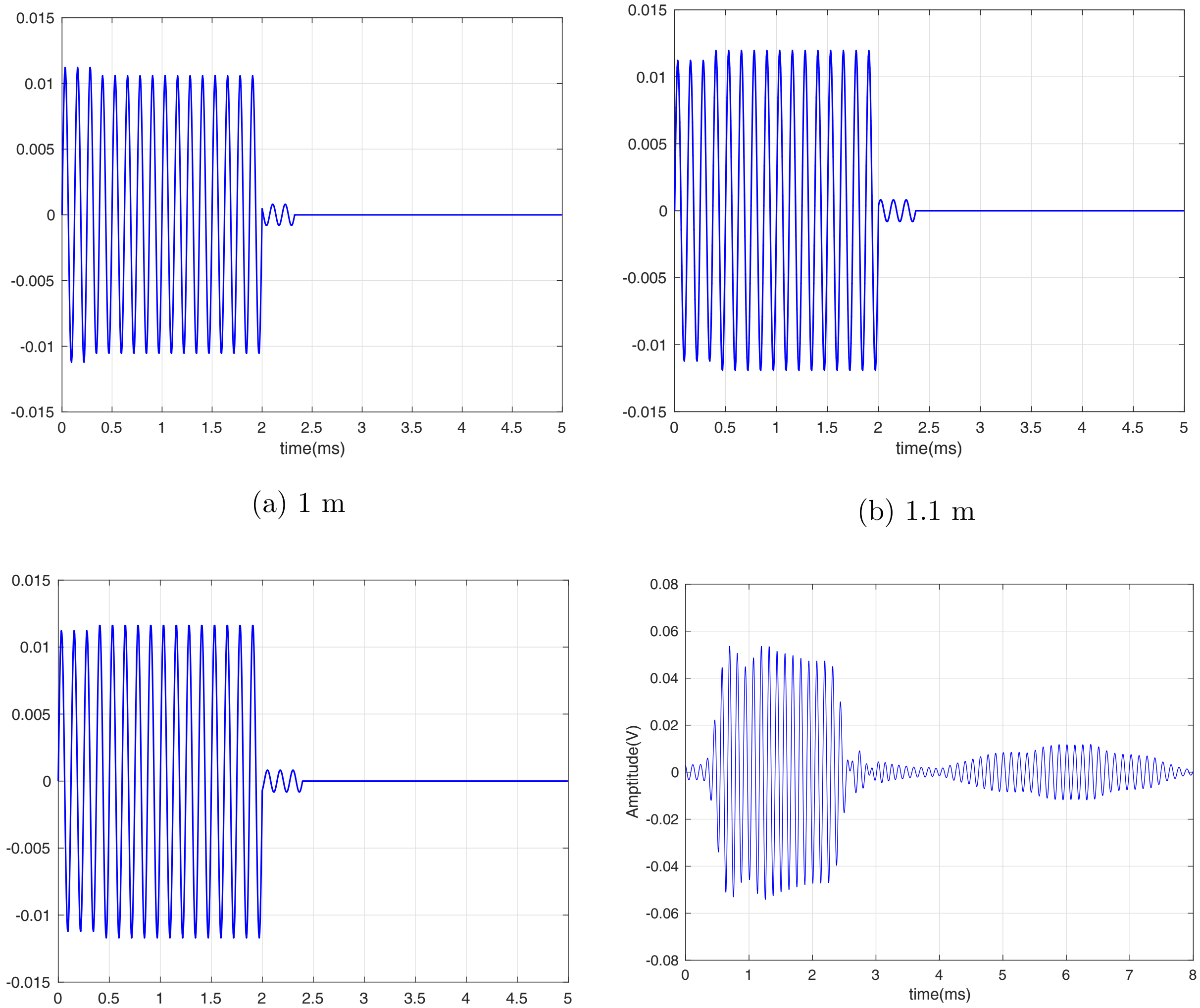

(a) 1 m

(b) 1.1 m

(c) 1.2 m

(d) Real receiving signal of the hydrophone No. 2

FIG. 11. Comparison of simulated receiving signals of the receiver at different heights with the real receiving signal of the hydrophone No. 2 at a depth of 1 m. The simulations were run with measured bottom acoustic properties.

of signal level with different receiver heights is less than 0.6 dB, which demonstrates that the surface-bottom (SB) bounce can be neglected for a slow bottom with a sound speed ratio 0.973.

V. EXPERIMENTAL RESULTS

In this section, details of the experimental data are presented. A typical measurement consisted of 100 pulses transmitted with an interval of 2 s between pulses. A train of 100 pulses at one frequency was transmitted, followed by 100 pulses at the next frequency and repeated until all of the considered frequencies were covered. Therefore, the signals at different frequencies were acquired under almost the same environmental conditions at each incident grazing angle. For each measurement, when the grazing angle is adjusted in place, signals at 4, 8 and 15 kHz were transmitted. Table.I contains details of the experiment, including the grazing and scattering azimuth angles (as computed in Sec. IV C and reported for hydrophone No. 2), the wave direction, significant wave height, wave period and wind speed. The scattered azimuth is relative to the wave direction as shown in FIG. 7. The detailed environmental conditions are illustrated in Table.I.

Scattered and coherently reflected components are contained when a pulse interacts with sea surface. The reflected component is dominant for a flat surface near specular direction. The experiments were conducted at three incident grazing angles. The HLA is near the specular direction at a grazing angle of 13°. To compare the difference between scattering strength under different conditions at different frequencies, the reflected components have been removed from the received signals. The scattering strength determined from the signal received by hydrophone No. 2 of the HLA at each frequency of each incident grazing angle from 25th October to 30th October, 2019 is shown in FIG. 12. Error bars represent uncertainty of scattering strength, which includes statistical uncertainty and sys-

TABLE I. Environmental parameters during the experiments

date	source depth(m)	$\theta_i(^\circ)$	$\theta_s(^\circ)$	wave direction (°)	scattered azimuth(°)	significant wave height(m)	significant wave period (s)	wind speed (m/s)
Oct.25	9.0	13	168.7	76	167.5	0.3	5.5	10.3
	10.1	20	170.0	118	125.5	0.3	5.4	9.3
	10.1	30	171.3	114	129.5	0.3	5.5	9.5
Oct.26	9.0	13	168.7	90	153.5	0.2	6.6	3.5
	10.4	20	169.3	100	143.5	0.2	6.2	3.1
	10.4	30	171.0	103	140.5	0.2	5.3	2.0
Oct.28	7.2	13	172.0	152	91.5	0.5	3.4	7.9
	7.0	20	173.6	139	104.5	0.4	3.4	7.3
	7.3	30	174.0	140	103.5	0.4	3.8	7.4
Oct.29	7.3	13	171.9	120	123.5	0.1	4.3	5.9
	6.9	20	173.7	133	110.5	0.1	4.0	6.1
	6.9	30	174.3	118	125.5	0.1	4.4	7.8
Oct.30	7.9	13	170.9	123	120.5	0.3	3.2	1.2
	7.5	20	173.1	115	128.5	0.2	3.4	2.0
	7.4	30	173.9	113	130.5	0.2	3.7	2.0

tematic uncertainty. The systematic uncertainty includes uncertainty of source level, source beam pattern, hydrophone sensitivity, and approximation of spherical spreading. For different incident grazing angles, the fluctuation of scattering strength under different conditions decreases as the frequency increases.

For a comprehensive analysis of the surface forward scattering experiments at different frequencies, the surface roughness parameter is used to distinguish the coherent and incoherent components. The surface roughness parameter χ is useful for classification of roughness regimes, given by (Thorsos, 1984)

$$\chi = \frac{2\pi h\left(\sin\theta_i + \sin\theta_s\right)}{\lambda} \tag{13}$$

where h is the RMS surface wave height related to the significant wave height H by $H = 4h$, and λ is the acoustic wavelength. For $\chi \leq 0.5$, the surface interaction is principally coherent (reflection); for $\chi \geq 2$, incoherent (scattering) dominates. At intermediate values of χ, the two components can be comparable (Thorsos, 1984). The scattering strength of hydrophone No. 2 of the HLA at angles of 30° under different conditions are shown in FIG. 13. The receivers are away from the specular direction when incident grazing angle is at 30°. The roughness parameter χ is approximately 0.5 at a frequency of 4 kHz for all environmental conditions, and coherent reflection is the dominant part of the surface interaction. It is equal or greater than 1 at a frequency of 15 kHz. The coherent components have some impact on the surface interaction at all frequencies. Here the coherent components have been removed from each ping by subtracting an average over an ensemble of all pings for each measurement in FIG. 13. The receivers are near the specular direction when the incident grazing angle is at 13°, and the surface interaction is primarily coherent or reflection. Reflection can be

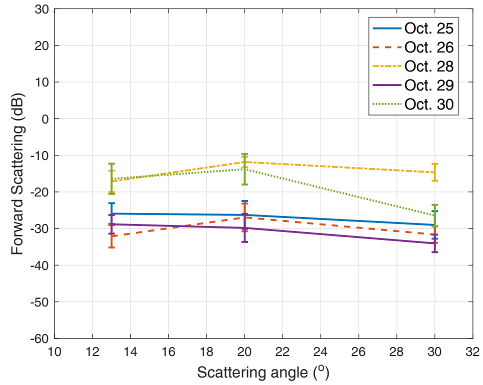

(a) f = 4 kHz

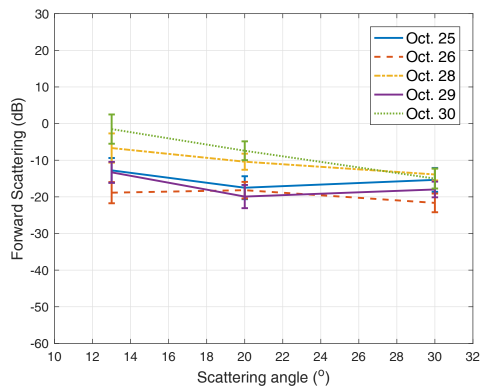

(b) f = 8 kHz

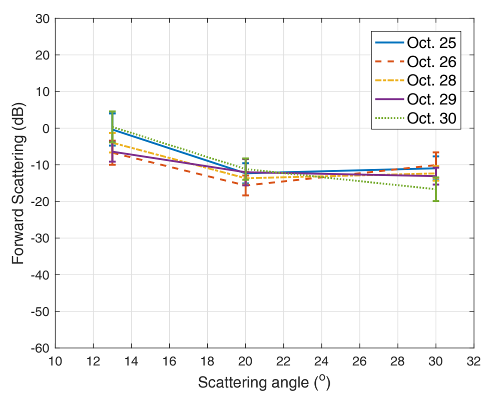

(c) f = 15 kHz

FIG. 12. Forward scattering intensity at different frequencies of different grazing angles. In each figure, forward scattering strength from hydrophone No. 2 of the HLA measured at different times are put together with uncertainty. (a) 4 kHz; (b) 8 kHz; (c) 15 kHz.

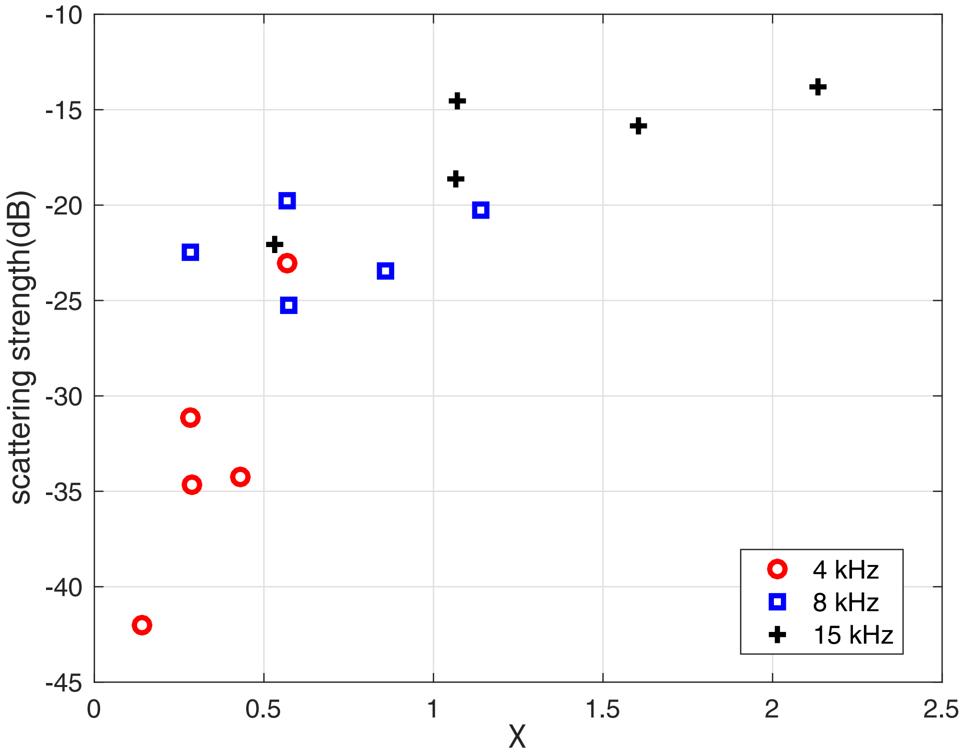

FIG. 13. Scattering strength versus the surface roughness parameter χ at a grazing angle of 30° for 4 kHz (circles), 8 kHz (squares) and 15 kHz (crosses).

described by a coherent reflection loss, RL_{coh}, which is given in the Kirchhoff approximation by

$$RL_{coh} = -10 \log \left(e^{-\chi^2} \right) \tag{14}$$

The reflection loss is restricted to the specular condition with reflection grazing angle equal to incident grazing angle(Thorsos, 1984). Theoretical coherent reflection loss given in the Kirchhoff approximation with measured environmental parameters is compared with the experimental data in FIG. 14. The experimental results show a good approximation for 4 kHz when $\chi < 0.5$. The roughness parameter increases as the frequency increases, with χ

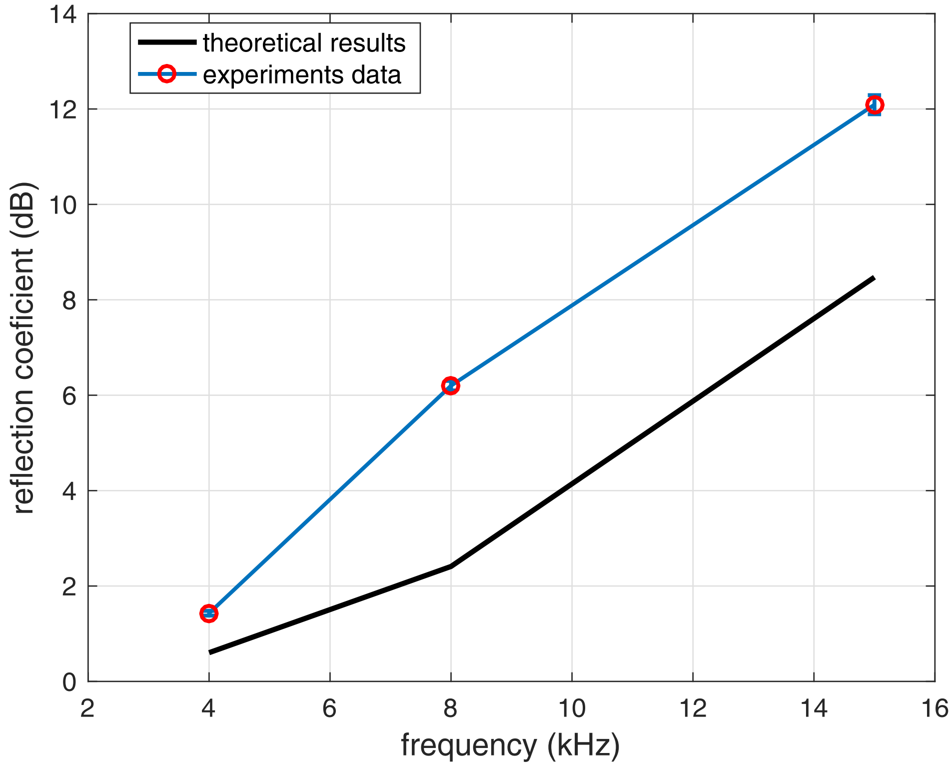

FIG. 14. Theoretical coherent reflection loss compared with experiments data at grazing angle of 13° near specular direction for 4 kHz, 8 kHz and 15 kHz.

equal to or larger than 1 for 8 kHz and 15 kHz. The error between theoretical results and experimental data increases as the roughness parameter increases.

Scattering strength across all five hydrophones of the HLA are averaged over all of the environmental conditions to obtain a single value for each frequency. The results at a grazing angle of 30° under different environmental conditions are plotted as the incident azimuth changes, in FIG. 15, to evaluate the impact of wave direction on the forward scattering. The incident azimuth is relative to wave direction defined in FIG. 7. The scattering strength increased as the incident azimuth approached 90°, corresponding to a wave direction perpendicular to the plane of the transducer and the HLA.

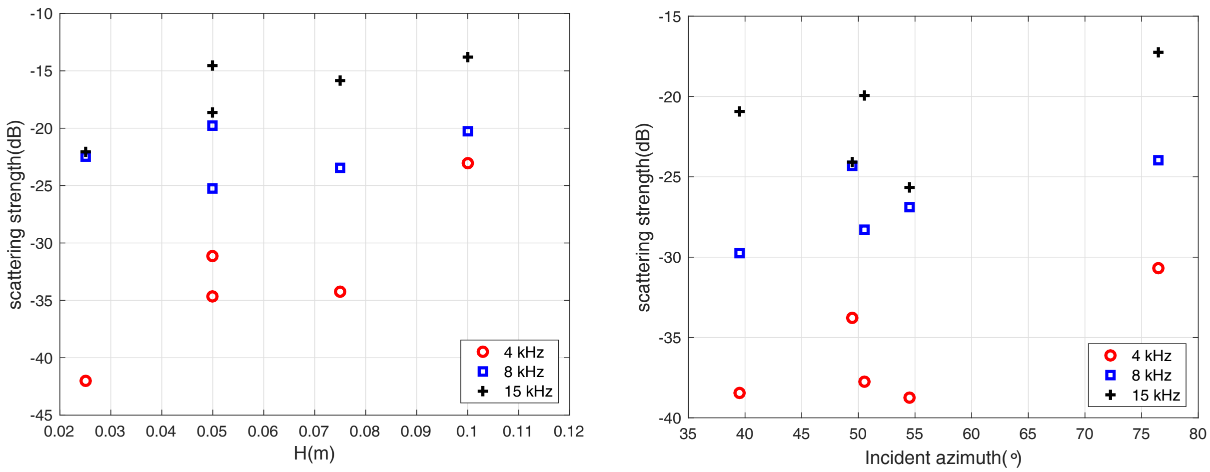

(a) Averaged scattering strength versus rms wave height

(b) Averaged scattering strength across the HLA versus incident azimuth

FIG. 15. Averaged scattering strength across the HLA versus incident azimuth and RMS wave height at a grazing angle of 30° for 4 kHz (circles), 8 kHz (squares) and 15 kHz (crosses).

The variation of scattering strength is fairly small as the RMS wave height changed at frequencies of 8 kHz and 15 kHz as shown in FIG.15(a). However, it increased as the incident azimuth changed from 40° to 80° as shown in FIG.15(b). This shows that the wave direction has a significant effect on the surface forward interaction.

VI. CONCLUSIONS

We conducted a series of forward acoustic scattering experiments where signals at 4, 8 and 15 kHz with different incident grazing angle of 13°, 20° and 30° were transmitted. The source level and beam pattern of the PAS at different ranges were calibrated before the experiments. The calibration results at ranges 20, 30 and 35 m were used to calculate the forward scattering strength at different incident grazing angles. Bistatic forward scattering strength is derived from a general case scattering intensity and an analytical expression of ensonified area is given. The results show that at different incident grazing angles, the fluctuation of the scattering strength under different conditions decreases as the frequency increases, and the wave direction has a significant effect on the surface forward scattering.

ACKNOWLEDGMENTS

The authors would like to thank Professor Eric I. Thorsos and Dajun Tang based at the Applied Physics Laboratory of University of Washington for providing advice on the experiments and analysis of the scattering data, and Professor Victor Humphrey based at the University of Southampton for his insight into the parametric array calibration.

This research was supported by the National Natural Science Foundation of China (NSFC) (grants 41527809, 41706066,and 41676055); the Opening Fund of Qingdao National Laboratory for Marine Science and Technology (grant QNLM2016ORP0209); the Shandong Provincial Key Research and Development Program, China (grant 2016GSF115033); and the Taishan Scholar Project Funding (No. tspd20161007).

A.G.Voronovich. “Small slope approximation in wave scattering by rough surfaces,” Sov. Phys. J. ETP **62**(1), 65–70 (**1985**).

Axline, R., and Fung, A.. “Numerical computation of scattering from a perfectly conducting random surface,” IEEE Transactions on Antennas and Propagation **26**(3), 482–488 (**1978**).

Broschat, S. L., and Thorsos, E. I.. "An investigation of the small slope approximation for scattering from rough surfaces. part ii. numerical studies," J. Acoust. Soc. Am. **101**(5), 2615–2625 (**1997**).

Chan, T.-K., Kuga, Y., Ishimaru, A., and Le, C. T.. "Experimental studies of bistatic scattering from two-dimensional conducting random rough surfaces," IEEE transactions on geoscience and remote sensing **34**(3), 674–680 (**1996**).

Dahl, P. H.. "On the spatial coherence and angular spreading of sound forward scattered from the sea surface: Measurements and interpretive model," J. Acoust. Soc. Am. **100**(2), 748–758 (**1996**).

Dahl, P. H.. "On bistatic sea surface scattering: Field measurements and modeling," J. Acoust. Soc. Am. **105**(4), 2155–2169 (**1999**).

Dahl, P. H.. "High-frequency forward scattering from the sea surface: The characteristic scales of time and angle spreading," IEEE journal of oceanic engineering **26**(1), 141–151 (**2001**).

Dahl, P. H.. "Forward scattering from the sea surface and the van cittert–zernike theorem," J. Acoust. Soc. Am. **115**(2), 589–599 (**2004**).

Elliott, R.. "Beamwidth and directivity of large scanning arrays," first of two parts, The Microwave Journal, 53–60 (**1963**).

Ellis, D. D., and Crowe, D. V.. "Bistatic reverberation calculations using a three-dimensional scattering function," J. Acoust. Soc. Am. **89**(5), 2207–2214 (**1991**).

Gauss, R., Fialkowski, J., and Wurmser, D.. "A low-and mid-frequency bistatic scattering model for the ocean surface," in *Proceedings of OCEANS 2005 MTS/IEEE (**2005**)*, IEEE, pp. 1738–1744.

Gauss, R. C., Gragg, R. F., Wurmser, D., Fialkowski, J. M., and Nero, R. W., "Broadband models for predicting bistatic bottom, surface, and volume scattering strengths," Report No. NRL/FR/7100–02-10,042, Naval Research Laboratory (**2002**).

Kinney, W. A., and Zornig, J. G.. "The azimuthal dependence of bistatic surface scattering: A comparison between theory and experiment," J. Acoust. Soc. Am. **77**(4), 1403–1408 (**1985**).

Macaskill, C., and Kachoyan, B.. "Numerical evaluation of the statistics of acoustic scattering from a rough surface," J. Acoust. Soc. Am. **84**(5), 1826–1835 (**1988**).

Moffett, M. B., and Mellen, R. H.. "Model for parametric acoustic sources," **61**(2), 325–337 (**1977**).

Thorsos, E. I., "Surface forward scattering and reflection.," Report No. N00024-81-C-6042, APL-UW (**1984**).

Thorsos, E. I.. "The validity of the kirchhoff approximation for rough surface scattering using a gaussian roughness spectrum," J. Acoust. Soc. Am. **83**(1), 78–92 (**1988**).

Thorsos, E. I., and Broschat, S. L.. "An investigation of the small slope approximation for scattering from rough surfaces. part i. theory," J. Acoust. Soc. Am. **97**(4), 2082–2093 (**1995**).

Thorsos, E. I., and Jackson, D. R.. "Thirty years of progress in theory and modeling of sea surface and seabed scattering," in *AIP Conference Proceedings 1495* (**2012**), pp. 127–149.

Urick, R. J., *Principles of underwater sound.* (Peninsula Publishing, 1983).

Voronovich, A. G., and Zavorotny, V. U.. "Full-polarization modeling of monostatic and bistatic radar scattering from a rough sea surface," IEEE Transactions on Antennas and Propagation **62**(3), 1362–1371 (**2013**).

Yu, S., Liu, B., Yu, K., Yang, Z., Kan, G., Feng, Z., and Zong, L.. "Measurements of midfrequency acoustic backscattering from a sandy bottom in the south yellow sea of china," IEEE Journal of Oceanic Engineering (99), 1–8 (**2017**).

Zornig, J. G.. "Bistatic surface scattering strength measured at short wavelengths," J. Acoust. Soc. Am. **63**(3), 758–767 (**1978**).